Thin–Walled Structures 224 (2026) 114697

Contents lists available at ScienceDirect

Thin-Walled Structures

journal homepage: www.elsevier.com/locate/tws

Full length article

Compact neural network-enhanced synthesis of a novel decoupled 2-DOF tilt stage based on graded auxetic and contracting honeycomb

Tingting Ye [a], Zhao Feng [b], Yangmin Li [a,*]

[a] Department of Industrial and Systems Engineering, The Hong Kong Polytechnic University, 999077, Hong Kong Special Administrative Region of China
[b] School of Robotics, Wuhan University, Wuhan, 430072, China

ARTICLE INFO

Keywords:
Compliant mechanisms
Auxetic metamaterial
Tilt stage
Piezoelectric actuator
Attention mechanism

ABSTRACT

Given the increasing demands for large strokes with low coupling for micro/nanomanipulation, a novel compact tilt stage is proposed based on the graded auxetic metamaterial to provide two degrees-of-freedom (DOFs) rotation motions in this paper. Firstly, graded auxetic and contracting structured honeycombs are designed with parallel combinations to provide amplified displacements driven by piezoelectric stacks, applying the orthogonal layering configuration with spatial distribution to alleviate rotation coupling. Compared with other tilt stages, larger rotation stroke and lower rotation coupling are yielded with compact dimension, attributed to intensive honeycomb structures. Then, the attention mechanism is involved in a compact neural network model to predict boundary conditions of the elliptical integral model, improving accuracy and simplifying derivation. Through sensitivity analysis and parametric optimization, the structural parameters are determined. To validate the effectiveness of design and modeling, the prototype of the proposed 2-DOF tilt stage is fabricated with the volume of 29*29*32 mm^3. Experimental results show the rotation strokes of 17.98 and 18.82 mrad, with the coupling ratio of 0.46% and 0.45%, respectively.

1. Introduction

Tilt stages are increasingly vital across applications requiring precision angular adjustment, such as rotary positioning stages for micro/nano manufacturing [1], polarization maintaining fiber alignment for optical instruments [2], and mirror scanning system [3]. Different from traditional rigid body mechanisms, compliant mechanisms are typically composed of rigid segments and flexure segments, in which flexure segments play the role of motion transmission joints or connections through flexing and returning to their original shapes [4]. Apparently, no friction, wear, or backlash is presented at flexure segments, bringing characteristics such as high precision, operational flexibility, structural compactness, and lightweight [5], leading to excellent application prospects in tilt stages. The integration of mechanical metamaterials, exhibiting physical properties not found in natural materials, such as stiffness, Poisson's ratio, etc., through specifically designed microstructural cells [6,7], into compliant mechanism design is an emerging, high-potential frontier. For example, regular auxetic re-entrant honeycomb, known to exhibit a negative Poisson's ratio, has been utilized to design a pneumatic needle driver based on compliant flexure beams, produced using additive manufacturing [8]. Concerning the application scenarios of tilt stages, larger stroke, smaller rotation coupling, and better space utilization are generally required, where the displacement direction conversion and programmable displacement transmission ratio of auxetic honeycomb demonstrate potential application value [9]. However, conventional regular auxetic honeycomb uniformly dissipates strain energy without concentrating or directing it to specific regions, resulting in limited displacement transmission efficiency, which may further be constrained by manufacturing precision.

Piezoelectric stacks are commonly employed in tilt stages for their compact size and high natural frequency, though limited stroke persists. As for motion amplification, asymmetry structures, and bridge-type structures were developed. An asymmetry structure with four identical inclined flexure beams was proposed by Wang et al. to provide 1-degree-of-freedom (DOF) rotation, showing a rotation range of 0.32 mrad [10]. Another asymmetry structure with J-shaped hinges and S-shaped hinges was designed based on the stiffness difference, showing the rotation range of 3.08 mrad [11]. A 1-DOF tilt stage was proposed by Yang et al. comprising spatially distributed P-layer and N-layer flexure-guided mechanisms, showing the rotation range of 9.23 mrad [12]. Besides, bridge-type structures were commonly employed, showing rotation ranges for 1.61–5.48 mrad [2,13,14]. As for motion decoupling, the configurations were dominated by planar orthogonal arrangements. A planar configuration of four identical modules

* Corresponding author.
E-mail addresses: tilda.ye@connect.polyu.hk (T. Ye), fengzhao@whu.edu.cn (Z. Feng), yangmin.li@polyu.edu.hk (Y. Li).

https://doi.org/10.1016/j.tws.2026.114697
Received 13 November 2025; Received in revised form 23 January 2026; Accepted 19 February 2026
Available online 20 February 2026

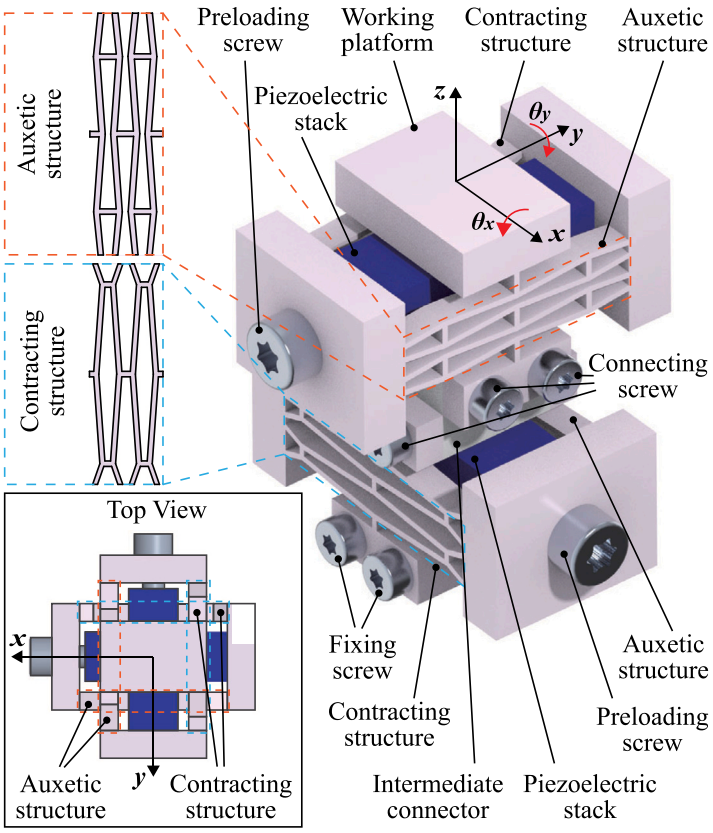

Fig. 1. Illustration of the proposed 2-DOF tilt stage based on graded auxetic metamaterial.

arranged orthogonally was proposed by Zhang et al. to yield 2-DOF rotation motions of travels of 1.61 mrad and coupling ratio of 3.93% [13]. Moreover, Hooke flexure hinges were proposed by Liang et al. with planar distributed configuration of two orthogonal identical bridge-type amplifiers, in which the rotation strokes were observed as 2.12 mrad with coupling ratio of 2.09% [2]. Similar configuration of four orthogonal identical bridge-type amplifiers was proposed by Jing et al. for a larger stroke [14], showing the rotation stroke of 5.48 mrad. Overall, inevitable coupling rotations are induced by planar orthogonal configurations for 2-DOF tilt stages.

To map structural parameters to mechanical performances, extensive research has been conducted with respect to analytical modeling methods. Pseudo-rigid body method can simplify the modeling problems of compliant mechanisms into the counterparts of rigid mechanisms [15]. However, inevitable deviations arise from overestimating deformations of compliant segments and oversighting deformations of pseudo-rigid segments for the pseudo-rigid body method, in which the prediction accuracy decreases as the deformation increases [5]. Besides, it shows insufficient generalization for compliant mechanisms and metamaterials with specified boundary conditions, such as structures with multiple flexure beams sharing one rotation connection [16]. Other modeling methods with better accuracy have also been studied for compliant mechanisms with distributed compliance based on Bernoulli–Euler beam theory and Timoshenko beam theory, such as elliptical integral solutions [17,18], beam constraint models [19,20], shooting method [21], etc. Shear deformation and moment of inertia are neglected in Bernoulli–Euler beam theory, making it applicable to flexure beams whose length significantly exceeds the in-plane width. Although shear deformation and moment of inertia are taken into account, the cross-sectional plane perpendicular to the neutral axis of the beam is considered not to bend during deformation in Timoshenko beam theory, making it suitable for short and thick beams. Combined with the chain algorithms, the application of Timoshenko beam theory is expanded to slender flexure beams with large deformations [22,23].

To improve modeling accuracy, simplify derivation difficulty, and increase method generalization, data-driven alternatives that can dig out and reconstruct relationships between input and output sequences in datasets show great potential in synthesizing compliant mechanisms with complex geometries and unconventional features [24]. Deep neural networks (DNNs) can establish linear or nonlinear relationships between output layers and input layers through large amounts of mathematical functions, in which the datasets are widely generated based on FEA simulations [25–27]. The synthesis process typically depends on large-scale datasets provided by the huge design domain, which is generated by numerous structural parameters and their dominant performances. However, high computational costs are triggered due to a large number of FEA simulations, hidden layers, and network connections. Besides, low model interpretability can be provided by FEA-based DNN models. On the other hand, some trials are also addressed to compensate for the modeling deviations in pseudo-rigid body methods through dynamic estimation of characteristic radius factors and stiffness coefficients. For example, data fitting were employed based on polynomial functions to estimate the aforementioned parameters of pseudo-rigid body methods for approximating the modeling results based on Bernoulli–Euler beam theory [28], FEA simulations, and experiments [29]. Moreover, a DNN model was adopted based on datasets generated by FEA simulations for the counterparts of the modified pseudo-rigid body model [16].

In short, the methodological research gaps for synthesizing 2-DOF tilt stage can be summarized as follows: (i) Conventional compliant mechanisms generally sacrifice structural compactness when obtaining a large amplification ratio, and some instances may exhibit unavoidable coupling motions, such as lever amplifiers; (ii) Regular auxetic honeycomb uniformly dissipates strain energy without concentrating or directing it to specific regions, resulting in limited displacement transmission efficiency; (iii) Analytical modeling is hard to derive for complex geometry, and FEA-based dataset generation leads to low

model interpretability. Motivated to develop a novel 2-DOF tilt stage with compact structure, large travel, and low coupling, the contributions of this paper can be summarized as follows: (i) An orthogonal layering configuration with spatial distribution is proposed for low coupling of tilt stage. (ii) A novel amplifying mechanism is proposed based on pairs of graded auxetic and contracting structured honeycomb for a larger stroke and a smaller volume, wherein the displacement amplification ratio can be improved through the directional strain concentration. (iii) Attention mechanism is involved in a compact neural network model to improve model accuracy and simplify derivation.

The remainder of this paper is organized as follows. The conceptual design of the proposed tilt stage is stated in Section 2 to introduce the mechanical composition and working principle. Section 3 presents the methodology to fulfill the kinetostatic modeling and dynamic modeling, as well as sensitivity analysis and parametric optimization. Simulation and experimental validations are conducted in Section 4. At last, the completed works are summarized and discussed in Section 5.

2. Conceptual design

As shown in Fig. 1, a novel tilt stage with two rotational DOFs θ_x and θ_y around axes x and y is proposed based on graded auxetic metamaterial, in which the working platform is arranged on the xy plane. The proposed tilt stage is composed of two modules of identical topology, one on the upper layer and one on the lower layer, which are orthogonally connected by four screws through the intermediate connector. The upper module is connected to the working platform above with flexures, and the lower module is connected to the base below with two fixing screws. For each module, a piezoelectric stack assembled by a preloading screw, an auxetic structure performing negative Poisson's ratio, and a contracting structure performing positive Poisson's ratio are included.

To reveal the working principle of the proposed tilt stage, the transmission of displacements can be described as follows. Taking the upper module as an example, the polarization direction of the piezoelectric stack is along the y-axis, that is, the input displacement is provided along the y-axis under voltage driving, wherein the auxetic structure and the contracting structure are arranged symmetrically on both sides of the piezoelectric stack with respect to the yoz plane, as shown in Fig. 2(a). The auxetic structure and the contracting structure are connected in parallel with piezoelectric stack, which can receive same linear input displacements in the y-axis. As for the auxetic structure based on re-entrant honeycombs, the negative Poisson's ratio can be exhibited with stretched deformation, resulting in the output displacement along the $+z$ direction, as shown in Fig. 2(b). On the contrary, the positive Poisson's ratio can be exhibited by the contracting structure based on convex honeycombs, leading to the output displacement along the $-z$ direction through stretched deformation along the y-axis, as shown in Fig. 2(c). Hence, the rotation around the y-axis of the working platform can be delivered by the upper module, engendering the orthogonal rotation around the x-axis by the lower layer accordingly.

In particular, planar graded auxetic honeycombs are engineered to achieve a larger absolute Poisson's ratio, i.e., amplified output strokes. Whereas conventional uniform auxetic honeycomb (with identical unit parameters: thickness $t_i = t_o$, cell length $l_i = l_o$, re-entrant angle $\alpha_i = \alpha_o$) dissipates strain energy uniformly, leading to limited displacement transmitting efficiency. The proposed graded auxetic honeycombs (with different unit parameters: thickness $t_i \neq t_o$, cell length $l_i \neq l_o$, re-entrant angle $\alpha_i \neq \alpha_o$) strategically concentrate strain energy toward output ends through deliberate different parameters, wherein the displacement amplification ratio can be improved through the directional strain concentration. The output strokes of the contracting structure based on the graded convex honeycombs can also be amplified compared to regular counterparts by analogy.

Taking both the required performance and the prototyping constraints into account, the objective performances of the desired tilt stage can be determined as follows. At first, gaps should be reserved to arrange the selected piezoelectric stacks (PSAs, model: Coremorrow Pst150/7*7/20, maximum driving voltage: 150 V, stroke: 20 μm, resonant frequency: 50 kHz, stiffness: 120 N/μm, thrust: 3500 N). Then, digital light processing, an area-wide photopolymerization technology, is employed for fabrication, achieving ±25 μm dimensional accuracy with a maximum manufacturing volume of 30*30*40 mm^3 within budget constraints. Limited by the processing accuracy, the unavoidable difference between the output displacements of the auxetic structure and the contracting structure should be as small as possible to reduce the coupling displacement of the working platform in the z direction. On this basis, the working stroke of the tilt stage should be maximized with minimized volume, wherein higher available speed could be better for higher efficiency.

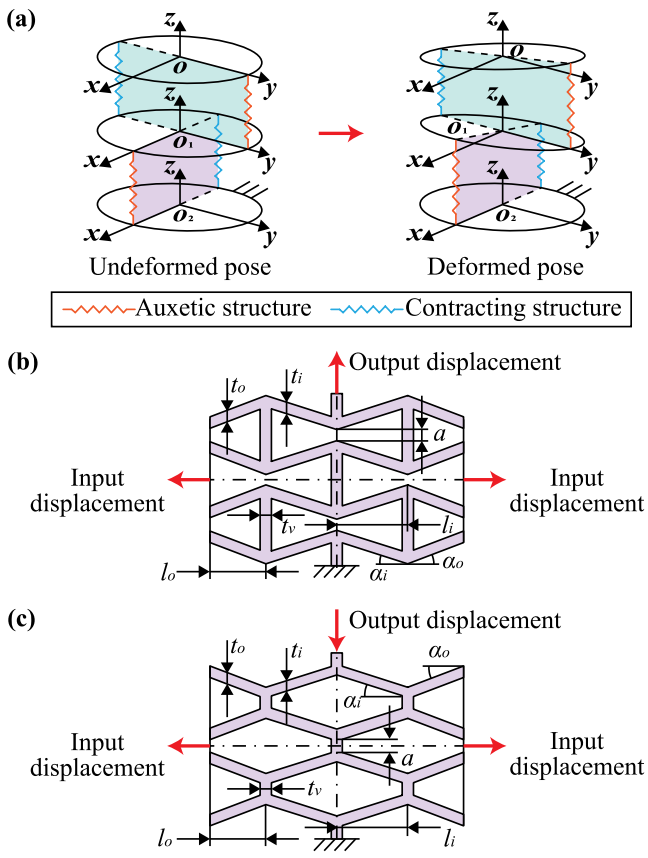

Fig. 2. Principle scheme of the proposed tilt stage: **(a)** undeformed and deformed poses, **(b)** auxetic structure based on graded re-entrant honeycombs, and **(c)** contracting structure based on graded convex honeycombs.

3. Characteristic analysis

To characterize kinetostatic and dynamic performance, the auxetic and contracting structures are idealized as repeating elemental cells, as shown in Fig. 3(a), each comprising two vertical beams and one inclined beam. Bending deformation in the vertical beams can be too small to be ignored due to the symmetric configuration. Due to the symmetric configuration, bending deformation of vertical beams could be too small to be ignored. Consequently, elemental cell motion is governed by bending deformation of inclined beams, as well as axial deformation of inclined beams and vertical beams.

3.1. Bending and axial deformations

The bending deformation of an inclined beam is analyzed, as shown in Fig. 3(b). The cross sections of the inclined beam are assumed

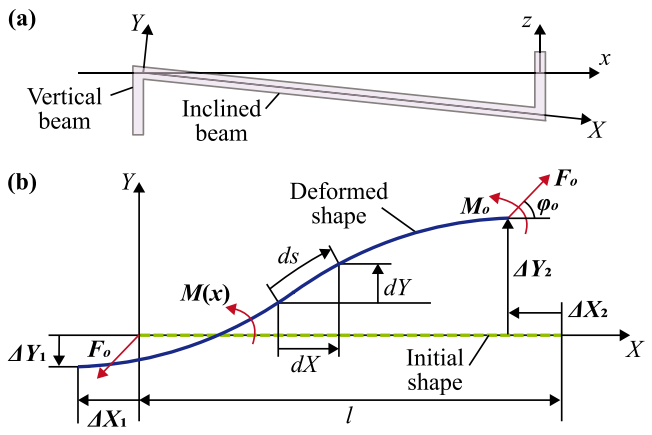

Fig. 3. Theoretical modeling of the proposed tilt stage: **(a)** elemental cell of auxetic/contracting structure, and **(b)** deformation of inclined beam.

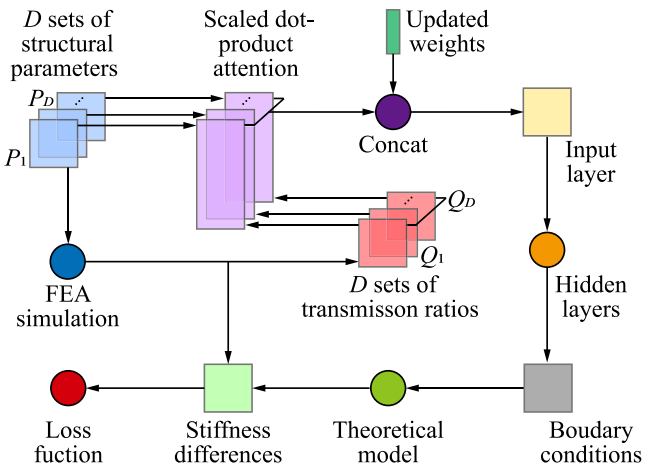

Fig. 4. Framework of compact neural network-enhanced model.

to be always perpendicular to the neutral layer during deformation. According to Bernoulli–Euler beam theory, the governing equation can be represented as:

$$EI\frac{d\phi}{ds} = M_o - F_oX\sin\varphi_o + F_oY\cos\varphi_o, \tag{1}$$

where M_o refers to the moment; E refers to Young's modulus; I refers to the moment of inertia; s and ϕ refer to arc length and inclined angle of beam; F_o and φ_o refer to external force and its inclined angle.

For axial deformation, Hooke's law is used to establish the linear relationship between the applied force and strain through the product of Young's modulus and the cross-sectional area. With geometry relationship, it can be established combining bending and axial deformations as:

$$\int_0^l \cos\phi ds + \int_0^l \frac{F_o}{EA_i}\cos(\varphi_o-\phi)\cos\phi ds = l + \Delta X_1 - \Delta X_2, \tag{2}$$

and

$$\int_0^l \sin\phi ds + \int_0^l \frac{F_o}{EA_i}\cos(\varphi_o-\phi)\sin\phi ds = -\frac{l_v F_o\sin\varphi_o}{EA_v} + \Delta Y_1 + \Delta Y_2, \tag{3}$$

where A_i and A_v refer to cross-sectional areas of inclined and vertical beams.

To express the tilt angle $\phi(s)$ along the arc length, the elliptical integrals are introduced for the closed-form solutions. In short, the dimensionless force can be derived as:

$$\sqrt{\frac{F_o l^2}{EI}} = \int_{\lambda_1}^{\lambda_2} e_1(h,\lambda_2) - e_1(h,\lambda_1), \tag{4}$$

where $\lambda(s)$ refers to a monotonically changing variable related to tilt angle $\phi(s)$; λ_1 and λ_2 refer to the value of $\lambda(0)$ and $\lambda(l)$; h can be obtained as:

$$\cos\left[(\phi-\varphi_o)/2\right] = h\sin\lambda; \tag{5}$$

e_1 refers to the first uncomplete elliptical integral as:

$$e_1(h,\lambda) = \int_0^{\lambda}\left[1-h^2\sin^2\delta\right]^{-1/2}d\delta. \tag{6}$$

Hence, the first and second terms on the left of Eq. (2) can be referred to bending and axial deformation along the x-axis, whose dimensionless pattern can be expressed as:

$$\cos\varphi_o(E_2-2E_1) - 2h\sin\varphi_o(\cos\lambda_2-\cos\lambda_1), \tag{7}$$

and

$$\int_{\lambda_1}^{\lambda_2}(2h^2\sin^2\lambda-1)\cos\phi d\lambda, \tag{8}$$

where

$$E_1 = e_1(h,\lambda_2) - e_1(h,\lambda_1),\quad E_2 = e_2(h,\lambda_2) - e_2(h,\lambda_1), \tag{9}$$

where

$$e_1(h,\lambda) = \int_0^{\lambda}\left[1-h^2\sin^2\delta\right]^{1/2}d\delta. \tag{10}$$

Then, the counterparts of Eq. (3) can be expressed as:

$$\sin\varphi_o(E_2-2E_1) - 2h\cos\varphi_o(\cos\lambda_2-\cos\lambda_1), \tag{11}$$

and

$$\int_{\lambda_1}^{\lambda_2}(2h^2\sin^2\lambda-1)\sin\phi d\lambda, \tag{12}$$

With preset boundary conditions, the transmission ratios and elastic constants in rotation about x- and y-axes can be calculated by several iterations. On this basis, the equivalent mass of each rotation DOF can be derived with the energy method. According to the Lagrangian dynamics equation, the resonant frequencies can be obtained, whose detailed derivation process can be referred to previous work [17].

3.2. Closed-form calculation

To determine the boundary conditions, the compact neural network is employed based on attention mechanism for improved model interpretability and reduced computational costs, as shown in Fig. 4. Given the designed topology, D sets of structural parameters are extracted from dimension domain, which is regarded as the input sequence $\mathbf{P}$ in the scaled dot-production attention. Substituting the structural parameters into FEA simulations, the corresponding transmission ratios can be obtained to establish query $\mathbf{Q}$. Consequently, the output sequence of each scaled dot-product attention layer can be established as:

$$Head_i(\mathbf{P}_i,\mathbf{Q}_i) = softmax\left(\frac{\mathbf{Q}_i\mathbf{P}_i^{\mathrm{T}}}{\sqrt{d_{\mathbf{P}}}}\right)\mathbf{P}_i\mathbf{W}_i^v, \tag{13}$$

where $i = 1, 2, \ldots, D$; $\mathbf{W}_i^v$ ia a learned weight matrix for each $Head_i$.

After D sets of calculation, the matrices obtained through Eq. (13) are concatenated as:

$$MultiHead(\mathbf{P},\mathbf{Q}) = Concat\left[Head_1, Head_2, \ldots, Head_D\right]. \tag{14}$$

After concatenation, a weight matrix $\mathbf{W}^a$ is applied for linear transformation to produce the weighted sequence of this multi-head attention model:

$$Output = MultiHead(\mathbf{P},\mathbf{Q})\mathbf{W}^a, \tag{15}$$

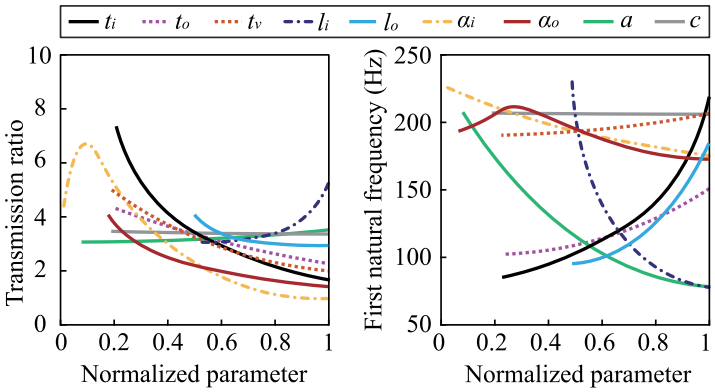

Fig. 5. Sensitivity analysis of main structural parameters.

Table 1
Ranges and optimized values of structural parameters.

Contracting	Range	Value	Auxetic	Range	Value
t_i (mm)	[0.4,1.5]	0.4	t_i (mm)	[0.4,1.5]	0.4
t_o (mm)	[0.4,1.5]	0.4	t_o (mm)	[0.4,1.5]	0.4
t_v (mm)	[0.4,1.5]	0.4	t_v (mm)	[0.4,1.5]	0.4
l_i (mm)	[4.5,10]	8.5	l_i (mm)	[4.5,10]	6.7
l_o (mm)	[1,4.5]	1.9	l_o (mm)	[1,4.5]	3.7
α_i (°)	[1,30]	4	α_i (°)	[1,30]	6
α_o (°)	[1,30]	19.5	α_o (°)	[1,30]	5.5
a (mm)	[0.5,5]	0.5	a (mm)	[0.5,5]	0.5
c (mm)	[2.5,12]	2.5	c (mm)	[2.5,12]	2.5

where the weight matrix $\mathbf{W}^a$ needs to be trained through another feedforward neural network.

After training, the equivalent stiffness can be obtained, using the mean square error of stiffness differences between theoretical and FEA models to construct the loss function. Each $Head_i$ operates independently, facilitating efficient training and inference to solve more complex relationships and interactions within the structural parameters and the boundary conditions. Besides, more comprehensive relationships can be captured, since multiple aspects can be learned through multiple heads.

3.3. Determination and sensitivity of structural parameters

Using the genetic algorithm, the parameter optimization is conducted for a larger transmission ratio and a smaller volume, which involves two conflicting objectives. Available ranges within the design space have been given in Table 1. All Pareto solutions are "equally good" with respect to the initial two objectives, necessitating the introduction of a higher-level criterion to make a definitive selection. Finally, the result with the largest first natural frequency in the Pareto front is selected, since a higher initial natural frequency implies a wider safe operating bandwidth and improved dynamic stability. It can be shown that the output rotation angles are 20.91 mrad in both DOFs, and the first natural frequency is 97.09 Hz.

To investigate the parametric sensitivity of the proposed graded auxetic structure, transmission ratios and first natural frequencies are calculated with respect to main parameters, as shown in Fig. 5. Apart from the current parameter varying within the design domain specified in Table 1, all other parameters adopt their optimized results. For example, when the parameter t_i varies from 0.4 to 1.5 mm, this "transmission ratio-t_i" curve is obtained with all other parameters held constant. Compared to conventional regular auxetic structures ($t_i = t_o$, $l_i = l_o$, $\alpha_i = \alpha_o$), it can be clearly observed that increasing l_i and decreasing l_o can significantly increase the displacement transmission ratio and decrease the first natural frequency. It can be demonstrated that the graded auxetic structure proposed in this paper ($l_i > l_o$) can effectively increase the output displacement within the same spatial range ($l_i + l_o$ = Constant). However, an excessive length difference will result in an extremely low first-order natural frequency, which must be considered in the design.

For transmission ratios, in-plane width of flexure beams t_i, t_o, and t_v are all negatively correlated, since the bending stiffness of a flexure beam is proportional to the cube of its in-plane width, leading to a dramatic rise in deformation resistance with increasing width. As a result, the input energy is stored primarily as elastic potential energy resisting bending deformation and in-plane constraints. Geometric parameters l_i, α_i, l_o, and α_o are presented with greater influences, in which the curve concerning α_i exhibits a single peak. When the angle is too small, axial tensile deformation far exceeds effective bending deformation, causing the transmission ratio to drop sharply. It is worth noting that a slight variation in the transmission ratio (−0.099) is still observable relative to the out-of-plane width c, which theoretically should be zero for planar structures. It can be attributed to Poisson's contraction in the out-of-plane direction constrained by internal materials, in which the induced non-zero out-of-plane normal stresses improve significantly with the increasing out-of-plane width, leading to energy loss.

For first natural frequencies, t_i, t_o, l_i, l_o, and a are presented with greater influence, while α_i, α_o, and t_v show much smaller spans. The in-plane thickness t_i and t_o of inclined beams are clearly more sensitive than the counterparts t_v of vertical beams. Since inclined beams dominate the output stiffness during bending deformation, while vertical beams participate almost exclusively in axial tension and compression deformation. Particularly, the curve concerning α_o exhibits a single peak, which is primarily due to the fact that at smaller angles, the vertical length of the rigid blocks on both sides of the structure needs to be longer, thereby increasing the equivalent mass. Since the out-of-plane thickness c is proportional to both volume and moment of inertia, it is nearly independent of the first natural frequency.

4. Validation

4.1. Simulation validation

To evaluate the static performance of the proposed tilt stage via FEA simulation, the model is meshed with 560 thousands of tetrahedral elements, with refinement applied to the flexure segments, i.e., auxetic and contracting structures. Output rotation angles across the x- and y-axes are extracted, using the upper module (polarized along the $y$axis) for y-axis actuation and the lower module (polarized along the x-axis) for x-axis actuation, respectively. For y-axis actuation, input displacements from 0 to 20 μm are applied for the upper module with fixed supports at the bottom. As shown in Fig. 6(a), the distribution of z-directional deformation under y-axis actuation is provided. Displacements of 152.3 μm along the $+z$ direction and 150.51 μm along the $-z$ direction can be observed at output ends of auxetic and contracting

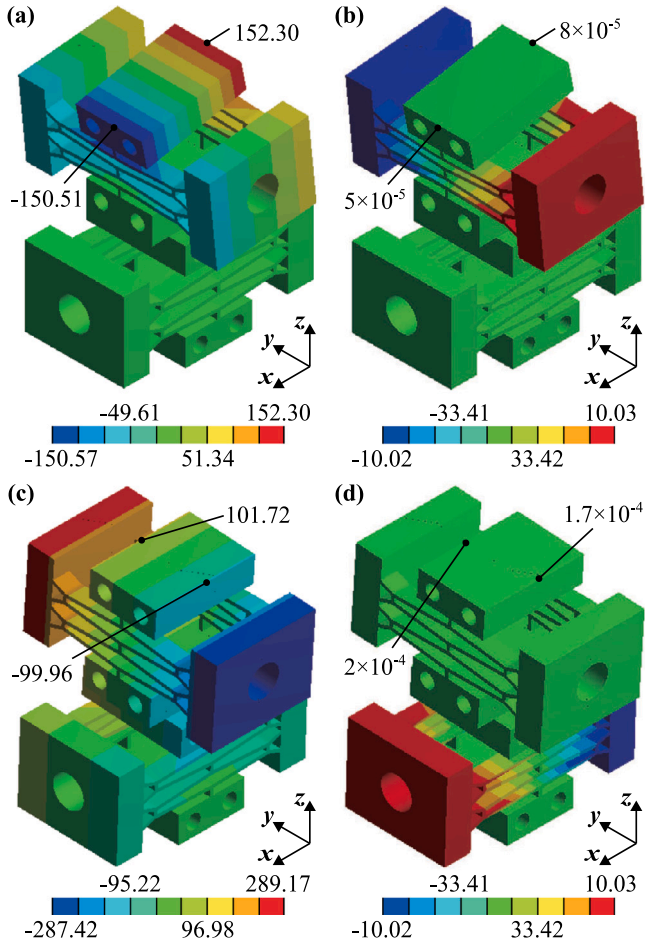

Fig. 6. Static simulation results (unit: μm): **(a)** z-directional deformation under y-axis actuation, **(b)** y-directional deformation under y-axis actuation, **(c)** z-directional deformation under x-axis actuation, and **(d)** x-directional deformation under x-axis actuation.

structures, respectively, resulting in the rotation angle across the y-axis of 20.19 mrad. The corresponding y-directional deformation is also solved, manifesting as quite small values and differences, as shown in Fig. 6(b). It can be inferred that there is ideally no coupling rotation across the x-axis, where the difference is due to the asymmetry of the model mesh. Similarly, the output rotation stroke across the x-axis can be yielded as 20.168 mrad under x-axis actuation, manifesting as rare coupling, as shown in Fig. 6(c) and (d).

To assess potential stress–strain nonlinearity from large deflections, stress distribution is explored within maximum input displacements. As shown in Fig. 7, the maximum stress is located at intersection points of inclined beams and vertical beams in the auxetic structure, with values of 9.03 MPa and 7.15 MPa, in which negligible nonlinearity exists on the stress–displacement curve. It can be seen that only single inflection points exist in the deformed shapes of the inclined beams throughout the entire working stroke, leading to the absence of buckling behavior.

As shown in Fig. 8, modal simulations are conducted to characterize the first six natural frequencies and their mode shapes. It can be observed that the first-order vibration mode is dominated by rotation about the y-axis at 90.69 Hz, and the second-order vibration mode is dominated by rotation about the x-axis at 164.41 Hz. Additionally, the third, fourth, and sixth-order vibration modes are dominated by rotation motions about the y, x, and z-axes at 390.46, 432.86, and 1116.32 Hz, while the fifth-order counterpart is along displacement in the z-axis at 505.57 Hz. Therefore, orthogonal motion decoupling can

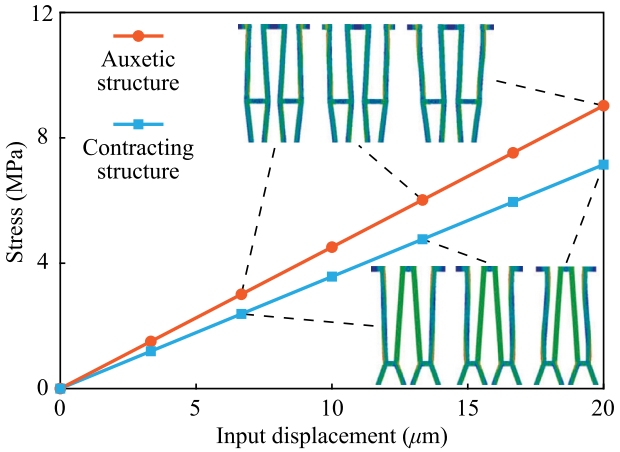

Fig. 7. Equivalent stress of the auxetic and contracting structures within input displacements from 0 to 20 μm.

be exhibited for the proposed tilt stage, accompanied by absent dense modes.

4.2. Experimental validation

As shown in Fig. 9, the experimental system is established. Physical prototype of the proposed 2-DOF tilt stage is manufactured via digital light processing with micro-nano photosensitive resin (model: Wenext HT210, Young's modulus: 4.3 GPa, tensile yield strength: 51 MPa). A feature resolution exceeding 50 μm with an accuracy of ±30 μm can be achieved, which is critical for precisely forming key flexible beams (minimum thickness 400 μm). In contrast, fused deposition modeling is constrained by material extrusion instability and incomplete path filling, leading to significant processing errors. Wire cutting precision is limited by electrode wire diameter (typically 0.1-0.3 mm), but our design incorporates not only thin beams but also enclosed voids formed by outer flexure beams, in which the inevitable fillet radii significantly impact dimensional accuracy. Besides, the high elongation of 15% at break of this material enables a safety margin for large-deformation tests, making it a preferred choice during the rapid prototyping validation stage.

Then, the rapid control system is built to generate analog voltage signals for the piezoelectric stacks and measure output displacements of the working platform. Control signals are originated from the LabVIEW-equipped personal computer (PC) to the server (model: NI cRIO-9504). Routed to the 16-bit digital-analog converter (DAC, model: NI-9264), the analog voltage signals are amplified via the dual-channel power amplifier (model: Coremorrow E01.B3), driving the piezoelectric stacks to provide input displacements for the tilt stage. Concurrently, output displacements at corners A, B, C, and D of the working platform are measured by laser sensors (model: Keyence LK-H025). Their analog outputs are digitized by a 12-bit analog–digital converter (ADC, model: NI-9201) and returned to the PC via the server.

To yield the transmission ratio between input and output displacements, ramp signals within the maximum travel ranges of piezoelectric stacks are applied. The median of adjacent corner measurements is used to calculate the output angles, as shown in Fig. 10(a). The maximum output rotation angles θ_x across the x-axis, and θ_y across the y-axis can be yielded as 17.98 and 18.82 mrad, respectively. Compared to simulation results, the discrepancies can be calculated as 12.18% and 7.27%. Nonlinearity from piezoelectric hysteresis can also be observed, with the maximum deviation of 0.84 mrad under the input velocity of 0.2 μm/s. As shown in Fig. 10(b), the harmonic frequency responses under independent x and y-axis actuations are generated with swept sine waves from 0.1 to 200 Hz to reveal the inherent dynamic coupling

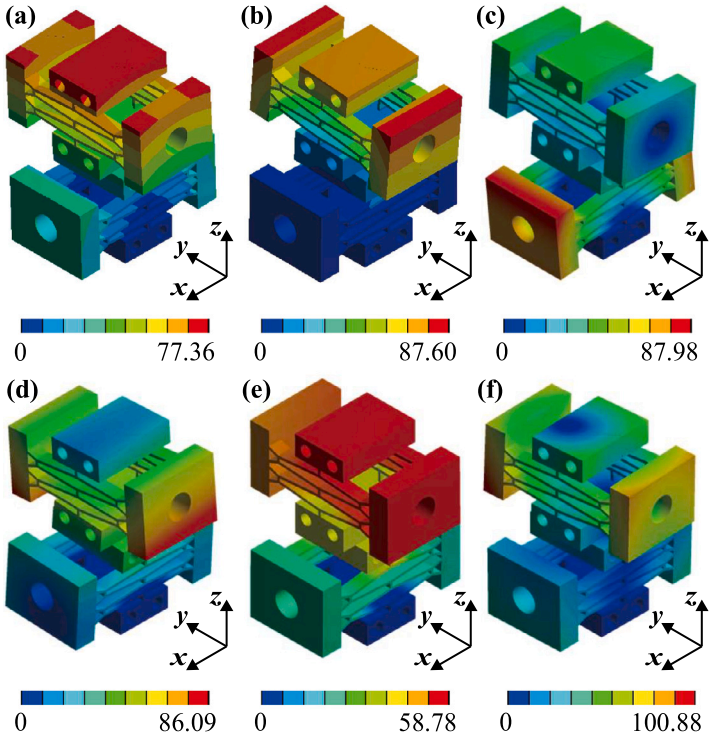

Fig. 8. Modal simulation results: **(a)** first mode shape at 90.69 Hz, **(b)** second mode shape at 164.41 Hz, **(c)** third mode shape at 390.46 Hz, **(d)** fourth mode shape at 432.86 Hz, **(e)** fifth mode shape at 505.57 Hz, and **(f)** sixth mode shape at 1116.32 Hz.

Table 2
Comparisons of mechanical properties with recent piezo-actuated tilt stages.

Indicator	[11]	[12]	[2]	[13]	This work
DOF(s)	θ_x	θ_x	θ_x, θ_y	θ_x, θ_y	θ_x, θ_y
NOAs	1	1	2	2	2
Volume (mm^3)	44*28*5.2	28*13*10	30*41*41	Φ54*18	29*29*32
Stroke (mrad)	3.08	9.23	2.12	1.61	18.82
Coupling ratio	/	0.54%	2.09%	3.93%	0.46%
Material	$AlSi_{10}Mg$	$AlSi_{10}Mg$	Al7075	Steel	Resin
FNF (Hz)	152	1086	580	356	87
SUR ($\mu rad/mm^3$)	0.48	2.54	0.04	0.04	0.70

* NOA: Number of actuator; FNF: First natural frequency; SUR: Space utilization ratio.

characteristics of the system. The solid curves represent y-axis-driven rotation θ_y and the corresponding parasitic rotation p_x, while dashed curves indicates the counterparts θ_x and p_y under x-axis actuation. The first two vibration modes can be presented at 81.14 Hz and 143.46 Hz. The first vibration mode is predominantly exhibited in rotation across the y-axis with 0.042% parasitic rotation across the x-axis, and the second vibration mode is predominantly exhibited in rotation across the x-axis with 0.006% parasitic rotation across the y-axis. Although the coupling is extremely slight, multi-input–multi-output or decoupling Control would be warranted for precise tracking or vibration suppression near these resonant frequencies. This observed coupling likely stems from inevitable geometric and material asymmetries introduced during manufacturing (e.g., slight variations in hinge thickness, assembly tolerances). Moreover, these discrepancies between two rotational DOFs can be primarily attributed to pressure from the upper module, according to a stroke test and a swept test with the removed upper module. The results show that the rotation angle θ_x and the first natural frequency can reach 18.53 mrad and 83.61 Hz, thereby substantiating the aforementioned viewpoint.

Sinusoidal responses under inputs of 10 Hz with amplitudes of 10 μm and offsets of 10 μm are obtained, as shown in Fig. 11. It can be observed that the maximum parasitic rotation travels across the x- and y-axes are 73.52 and 74.85 μrad under y-axis actuation and x-axis actuation, respectively. The corresponding coupling ratios are 0.46% and 0.45%, demonstrating excellent dynamic decoupling performance of the proposed tilt stage. No harmonic coupling issues can be observed in either dual-axis dynamic driving tests, despite such phenomena being present in some multi-DOF studies, which is likely attributed to the dense modes resulting from the structure's spatial symmetry. The mechanism proposed in this study features spatial asymmetry, thereby avoiding this issue.

Classic Bouc-Wen model [30] is involved to construct a feedforward inverse compensator concerning nonlinearity due to hysteresis. At first, full-stroke voltage-angle data is collected at a low frequency of 0.1 Hz to avoid the effects of creep at frequencies below 0.02 Hz and phase lag at frequencies above 1 Hz. Subsequently, the parameters [α, β, γ, η] of the Bouc–Wen model are identified using the genetic algorithm as [−0.6943, 1.9926, −0.6818, 1]. Then, the experimental results of sine wave reference displacement tracking under 0.1 Hz can be achieved, as shown in Fig. 12. Evidently, tracking errors caused by hysteresis can be effectively compensated by this model, in which the tracking error can be reduced to 0.249 mrad, representing a 60.27% decrease compared to open-loop testing.

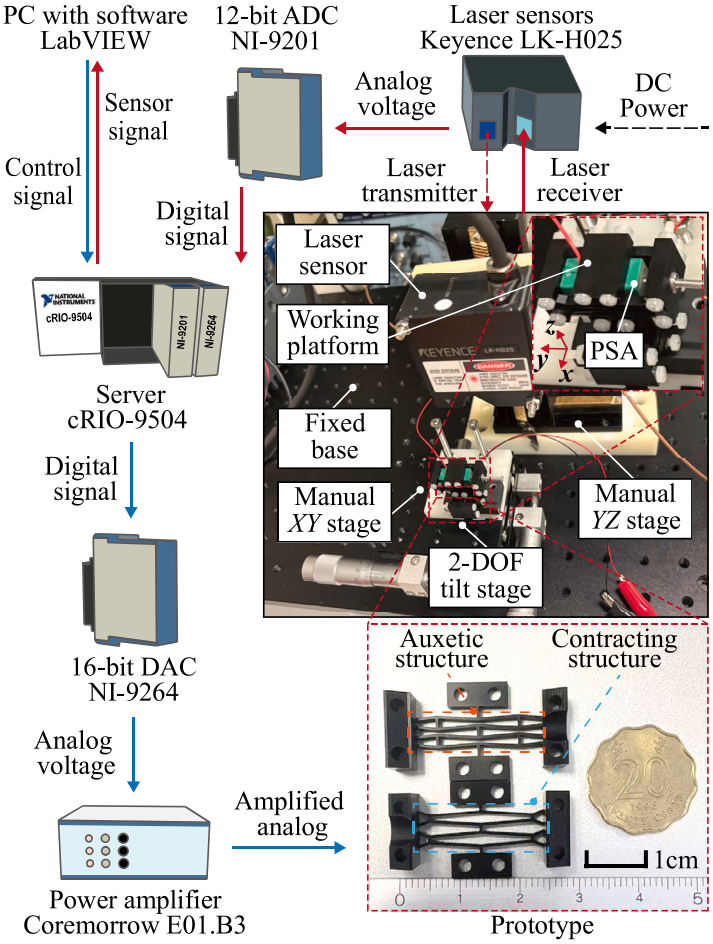

Fig. 9. Experimental system setup.

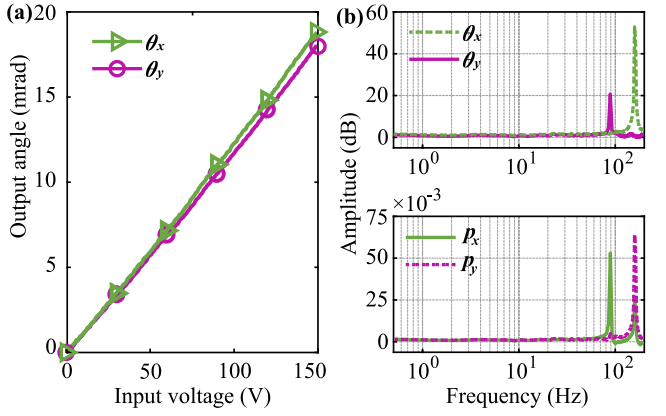

Fig. 10. Experimental results: **(a)** output angle-input voltage curve, and **(b)** harmonic frequency response.

4.3. Discussions

To evaluate the performance of the proposed tilt stage, the mechanical properties against recent related works are benchmarked in Table 2. Superior compactness, large stroke, low coupling, and high space utilization can be exhibited compared to recent piezo-actuated stages, which also verifies the effectiveness of design and optimization.

In addition, tilt stages driven by other actuators can also be discussed. A 2-DOF tilt stage driven by a hybrid-reluctance-force actuator was proposed based on a configuration of planar orthogonal arrangements with an outer diameter of 100 mm and a height of 70 mm, which could allow an angular range of ±52 mrad and an angular resolution of 5 μrad [31]. Although a larger input displacement can be provided by this hybrid-reluctance-force actuator than our adopted piezoelectric stack, a significantly lower space utilization ratio with a value of 0.19 can be derived with this stage, since displacement amplification and space compactness are rarely taken into account. Another tilt stage driven by voice coil motors was proposed based on three parallelogram compliant mechanisms arranged in a 120° spacing configuration, which could provide angular ranges of 51.9 and 44.3 mrad [32]. Similar larger input displacements are available, whereas more important poorer decoupling performance can be derived apart from similar lower spatial utilization.

Furthermore, some other metamaterials could also provide tensile-twist coupling motions, called chiral metamaterials [33,34]. It has been employed to achieve 1-DOF rotation θ_z through mounting the PSA externally at the input end of the spatially inclined beam, with the opposite plane serving as the output end (working platform) [35]. A rotation of 4.935 mrad can be provided under a size of $\Phi 32 * 68$ mm^3. Concerning the design requirements outlined in this manuscript, the primary issue with chiral structures lies in their difficulty in accommodating 2-DOF (θ_x and θ_y) working platforms. Due to the relative rotation between the input and output ends (θ_z), no stable geometry exists in the θ_x or θ_y direction for platform installation, and the low-coupling nature is also difficult to guarantee. Additionally, the external installation of the PSA is also necessitated, resulting in an increase in overall volume.

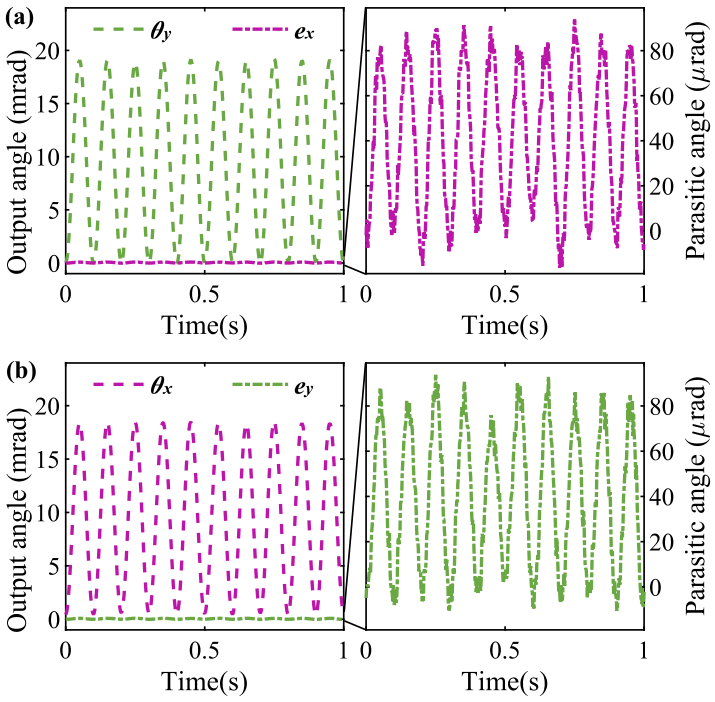

Fig. 11. Sinusoidal responses: **(a)** output angle θ_y and parasitic angle e_x under y-axis actuation of 10 Hz, and **(b)** output angle θ_x and parasitic angle e_y under x-axis actuation of 10 Hz.

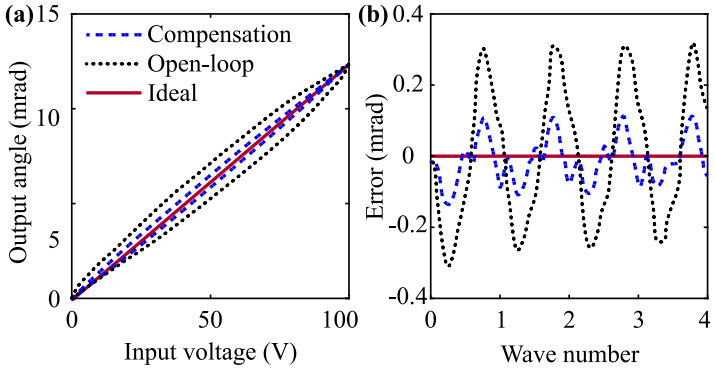

Fig. 12. Experimental results of sine wave reference displacement tracking: **(a)** output angle-input voltage curves, and **(b)** tracking errors.

5. Conclusions

Motivated by wider applications of angular adjustment in precision engineering, a novel decoupled 2-DOF tilt stage based on graded auxetic metamaterial was proposed in this paper. Composed of two piezoelectric stacks, two pairs of auxetic structure and contracting structure, intermediate connector, and two preloading screws, the proposed tilt stage was enabled with large deformation, attributed to intensive honeycomb structures of graded auxetic and contracting metamaterials. Due to orthogonal layering configuration with spatial distribution, excellent motion decoupling was provided. To characterize kinetostatic and dynamic performance, the auxetic and contracting structures are idealized as repeating elemental cells, each comprising two vertical beams and one inclined beam, whose motion is governed by bending deformation of inclined beams, as well as axial deformation of inclined beams and vertical beams. Introducing elliptical integrals, the attention mechanism is involved in a compact neural network model to predict boundary conditions of the elliptical integral model, improving model accuracy and reducing computational costs. This approach can be widely applied to complex structures with slender beam configurations, particularly in scenarios involving extremely high magnification ratios, but is less suitable for short-thick beams. Through sensitivity analysis and parametric optimization, the structural parameters are determined. To validate the effectiveness of design and modeling, the prototype of the proposed 2-DOF tilt stage is fabricated via digital light processing with a volume of 29∗29∗32 mm^3. Experimental results show the rotation strokes of 17.98 and 18.82 mrad, with coupling ratios of 0.46% and 0.45%, respectively. The first two-order vibration modes can be observed at 81.14 Hz and 143.46 Hz. Compared to recent piezo-actuated tilt stages, superior compactness, large stroke, low coupling, and high space utilization can be exhibited for this work, which also verifies the effectiveness of design and optimization. We must acknowledge that resin materials generally exhibit significant viscoelastic creep and stress relaxation issues, while machining high-precision complex thin beams with metal materials remains a common challenge within the field.

CRediT authorship contribution statement

Tingting Ye: Writing – original draft. **Zhao Feng:** Methodology, Investigation. **Yangmin Li:** Writing – review & editing, Supervision, Funding acquisition.

Declaration of competing interest

The authors declare that they have no known competing financial interests or personal relationships that could have appeared to influence the work reported in this paper.

Acknowledgments

This research was funded by the Research Impact Fund of Hong Kong (Grant No. R5047-22), National Natural Science Foundation of China (Grant No. 52405034), Hubei Provincial Natural Science Foundation of China (Grant No. 2024AFB126), and Knowledge Innovation Program of Wuhan-Shuguang Project (Grant No. 2023010201020252).

Data availability

Data will be made available on request.

References

[1] J. Ye, A. El Desouky, A. Elwany, On the applications of additive manufacturing in semiconductor manufacturing equipment, J. Manuf. Process. 124 (2024) 1065–1079, http://dx.doi.org/10.1016/j.jmapro.2024.05.054.
[2] C. Liang, F. Wang, Z. Huo, B. Shi, Y. Tian, X. Zhao, D. Zhang, A 2-DOF monolithic compliant rotation platform driven by piezoelectric actuators, IEEE Trans. Ind. Electron. 67 (2019) 6963–6974, http://dx.doi.org/10.1109/TIE.2019.2935933.
[3] D. Pechgraber, E. Csencsics, G. Schitter, Resonant rotational reluctance actuator for large range scanning mirrors, IEEE/ASME Trans. Mechatronics 28 (2023) 3573–3582, http://dx.doi.org/10.1109/TMECH.2023.3252940.
[4] J. Ling, T. Ye, Z. Feng, Y. Zhu, Y. Li, X. Xiao, A survey on synthesis of compliant constant force/torque mechanisms, Mech. Mach. Theory 176 (2022) 104970, http://dx.doi.org/10.1016/j.mechmachtheory.2022.104970.
[5] M. Ling, L.L. Howell, J. Cao, G. Chen, Kinetostatic and dy- namic modeling of flexure-based compliant mechanisms: a survey, Appl. Mech. Rev. 72 (2020) 030802, http://dx.doi.org/10.1115/1.4045679.
[6] Y. Wang, C. Chen, Y. Cheng, Multistable me- chanical metastructures: Classifications, architectures, characteristics and applications, Thin-Walled Struct. 216 (2025) 113613, http://dx.doi.org/10.1016/j.tws.2025.113613.
[7] C. Luo, C.Z. Han, X.Y. Zhang, X.G. Zhang, X. Ren, Y.M. Xie, Design, manufacturing and applications of auxetic tubular structures: A review, Thin-Walled Struct. 163 (2021) 107682, http://dx.doi.org/10.1016/j.tws.2021.107682.
[8] F. Schmitt, O. Piccin, B. Bayle, P. Renaud, L. Barbé, Inverted honeycomb cell as a reinforcement structure for building soft pneumatic linear actuators, J. Mech. Robot. 13 (2021) 011020, http://dx.doi.org/10.1115/1.4048834.
[9] A. Garg, A. Sharma, W. Zheng, L. Li, A review on artificial intelligence-enabled mechanical analysis of 3D printed and FEM-modelled auxetic metamaterials, Virtual Phys. Prototyp. 20 (2025) e2445712, http://dx.doi.org/10.1080/17452759.2024.2445712.
[10] G. Wang, Y. Yan, J. Ma, J. Cui, Design, test and control of a compact piezoelectric scanner based on a compound compliant amplification mechanism, Mech. Mach. Theory 139 (2019) 460–475, http://dx.doi.org/10.1016/j.mechmachtheory.2019.05.009.
[11] L. Zhang, P. Liu, P. Yan, A novel compact tilt stage with additive manufacturable spatial flexure mechanism driven by asymmetric stiffness, Mech. Mach. Theory 166 (2021) 104443, http://dx.doi.org/10.1016/j.mechmachtheory.2021.104443.
[12] Z. Yang, Y. Shi, P. Yan, A novel design of compact tilt stage with spatially distributed anti-symmetric compliant mechanism, Sensors Actuators A: Phys. 349 (2023) 113995, http://dx.doi.org/10.1016/j.sna.2022.113995.
[13] S. Zhang, Y. Liu, J. Deng, K. Li, Q. Chang, Development of a low capacitance two-axis piezoelectric tilting mirror used for optical assisted micromanipulation, Mech. Syst. Signal Process. 154 (2021) 107602, http://dx.doi.org/10.1016/j.ymssp.2020.107602.
[14] Z. Jing, M. Xu, B. Feng, Modeling and optimization of a novel two-axis mirror-scanning mechanism driven by piezoelectric actuators, Smart Mater. Struct. 24 (2014) 025002, http://dx.doi.org/10.1088/0964-1726/24/2/025002.
[15] L.L. Howell, S.P. Magleby, B.M. Olsen, J. Wiley, Handbook of Compliant Mechanisms, 2013, http://dx.doi.org/10.1002/9781118516485.
[16] T. Ye, Z. Feng, J. Ling, Y. Li, A novel w-shaped flexure-guided mechanism for high-frequency piezo-actuated micromanipulations, IEEE/ASME Trans. Mechatronics 30 (2025) 3781–3791, http://dx.doi.org/10.1109/TMECH.2024.3476332.
[17] T. Ye, J. Ling, X. Kang, Z. Feng, X. Xiao, A novel two-stage constant force compliant microgripper, J. Mech. Des. 143 (2021) 053302, http://dx.doi.org/10.1115/1.4048217.
[18] K. Xu, H. Liu, W. Yue, J. Xiao, Y. Ding, G. Wang, Kinematic modeling and optimal design of a partially compliant four-bar linkage using elliptic integral solution, Mech. Mach. Theory 157 (2021) 104214, http://dx.doi.org/10.1016/j.mechmachtheory.2020.104214.
[19] K. Wu, G. Zheng, G. Chen, Extending timoshenko beam theory for large deflections in compliant mechanisms, J. Mech. Robot. 15 (2023) 061012, http://dx.doi.org/10.1115/1.4056501.
[20] M. Ling, H. Zhou, L. Chen, Dynamic stiffness matrix with Timoshenko beam theory and linear frequency solution for use in compliant mechanisms, J. Mech. Robot. 15 (2023) 061002, http://dx.doi.org/10.1115/1.4056236.
[21] Y. Miao, J. Zheng, Optimization design of compliant constant force mechanism for apple picking actuator, Comput. Electron. Agric. 170 (2020) 105232, http://dx.doi.org/10.1016/j.compag.2020.10523.
[22] Y. Chen, S. Yao, M.Q.H. Meng, L. Liu, Chained spatial beam constraint model: A general kinetostatic model for tendon-driven continuum robots, IEEE/ASME Trans. Mechatronics 29 (2024) 105232, http://dx.doi.org/10.1109/TMECH.2023.3348510.
[23] F. Ma, G. Chen, Modeling large planar deflections of flexible beams in compliant mechanisms using chained beam-constraint-model, J. Mech. Robot. 8 (2016) 021018, http://dx.doi.org/10.1115/1.4031028.
[24] P. Jiao, A.H. Alavi, Artificial intelligence-enabled smart mechanical metamaterials: advent and future trends, Int. Mater. Rev. 66 (2021) 365–393, http://dx.doi.org/10.1080/09506608.2020.181539.
[25] F. Liu, X. Jiang, X. Wang, L. Wang, Machine learning-based design and optimization of curved beams for multistable structures and metamaterials, Extrem. Mech. Lett. 41 (2020) 101002, http://dx.doi.org/10.1016/j.eml.2020.101002.
[26] V.B. Dinh, N.L. Chau, N.T. Le, T.P. Dao, Topology-based geometry optimization for a new compliant mechanism using improved adaptive neuro-fuzzy inference system and neural network algorithm, Eng. Comput. 38 (2022) 5003–5032, http://dx.doi.org/10.1007/s00366-021-01552-y.
[27] N.L. Chau, N.T. Tran, T.P. Dao, A hybrid approach of density-based topology, multilayer perceptron, and water cycle-moth flame algorithm for multi-stage optimal design of a flexure mechanism, Eng. Comput. 38 (2022) 2833–2865, http://dx.doi.org/10.1007/s00366-021-01417-4.
[28] M. Jin, C. Ynchausti, L.L. Howell, Zero-curvature deformation properties and 3r pseudo-rigid-body model of large-deflection euler spiral beams, Mech. Mach. Theory 183 (2023) 105261, http://dx.doi.org/10.1016/j.mechmachtheory.2023.105261.
[29] B. Hargrove, A. Nastevska, M. Frecker, J. Jovanova, Pseudo rigid body model for a nonlinear folding compliant mechanism, Mech. Mach. Theory 176 (2022) 105017, http://dx.doi.org/10.1016/j.mechmachtheory.2022.105017.
[30] M. Rakotondrabe, Bouc-wen modeling and inverse multiplicative structure to compensate hysteresis nonlinearity in piezoelectric actuators, IEEE Trans. Autom. Sci. Eng. 8 (2011) 428–431, http://dx.doi.org/10.1109/TASE.2010.2081979.
[31] E. Csencsics, J. Schlarp, G. Schitter, High-performance hybrid-reluctance-force-based tip/tilt system: design, control, and evaluation, IEEE/ASME Trans. Mechatronics 23 (2018) 2494–2502, http://dx.doi.org/10.1109/TMECH.2018.2866272.
[32] P. Li, Y. Chen, C. Xie, Z. Xu, L. Lai, L. Zhu, Design, modeling, and control of a long stroke compliant tip-tilt-piston micropositioning stage driven by voice coil motors, Rev. Sci. Instrum. 95 (2024) 075001, http://dx.doi.org/10.1063/5.0203529.
[33] F. Lu, T. Wei, C. Zhang, Y. Huang, Y. Zhu, X. Rui, A novel 3d tetra-missing rib auxetic meta-structure with tension/compression-twisting coupling effect, Thin-Walled Struct. 199 (2024) 111764, http://dx.doi.org/10.1016/j.tws.2024.111764.
[34] T. Wei, F. Lu, C. Zhang, Y. Huang, X. Rui, Y. Zhu, Energy absorption of 3d assembled auxetic meta-structure with compression-twisting effect, Structures 73 (2025) 108482, http://dx.doi.org/10.1016/j.istruc.2025.108482.
[35] M. Xun, H. Yu, Y. Liu, J. Deng, S. Zhang, K. Li, A precise rotary piezoelectric actuator based on the spatial screw compliant mechanism, IEEE/ASME Trans. Mechatronics 28 (2022) 223–232, http://dx.doi.org/10.1109/TMECH.2022.3197454.